He–ThO(1Σ+) Interactions at Low Temperatures: Elastic and Inelastic Collisions, Transport Properties, and Complex Formation in Cold 4He Gas

He–ThO(1+) interactions at low temperatures: Elastic and inelastic collisions, transport properties, and complex formation in cold 4He gas

T. V. Tscherbul, E. R. Sayfutyarova, A. A. Buchachenko, and A. Dalgarno

Citation: J. Chem. Phys. **134**, 144301 (2011); doi: 10.1063/1.3575399
View online: http://dx.doi.org/10.1063/1.3575399
View Table of Contents: http://jcp.aip.org/resource/1/JCPSA6/v134/i14
Published by the American Institute of Physics.

He–ThO($^1\Sigma^+$) interactions at low temperatures: Elastic and inelastic collisions, transport properties, and complex formation in cold ^{4}He gas

T. V. Tscherbul,[1,2,a)] E. R. Sayfutyarova,[3] A. A. Buchachenko,[3] and A. Dalgarno[1,2]
[1]*Harvard-MIT Center for Ultracold Atoms, Cambridge, Massachusetts 02138, USA*
[2]*Institute for Theoretical Atomic, Molecular and Optical Physics, Harvard-Smithsonian Center for Astrophysics, Cambridge, Massachusetts 02138, USA*
[3]*Department of Chemistry, Moscow State University, Moscow 119991, Russia*

(Received 21 November 2010; accepted 20 March 2011; published online 8 April 2011)

We present an *ab initio* study of cold ^{4}He + ThO($^1\Sigma^+$) collisions based on an accurate potential energy surface (PES) evaluated by the coupled cluster method with single, double, and noniterative triple excitations using an extended basis set augmented by bond functions. Variational calculations of rovibrational energy levels show that the ^{4}He–ThO van der Waals complex has a binding energy of 10.9 cm^{-1} in its ground $J = 0$ rotational state. The calculated energy levels are used to obtain the temperature dependence of the chemical equilibrium constant for the formation of the He–ThO complex. We find that complex formation is thermodynamically favored at temperatures below 1 K and predict the maximum abundance of free ground-state ThO($v = 0$, $j = 0$) molecules between 2 and 3 K. The calculated cross sections for momentum transfer in elastic He + ThO collisions display a rich resonance structure below 5 cm^{-1} and decline monotonically above this collision energy. The cross sections for rotational relaxation accompanied by momentum transfer decline abruptly to zero at low collision energies (<0.1 cm^{-1}). We find that Stark relaxation in He + ThO collisions can be enhanced by applying an external dc electric field of less than 100 kV/cm. Finally, we present calculations of thermally averaged diffusion cross sections for ThO in He gas, and find these to be insensitive to small variations of the PES at temperatures above 1 K.
 [doi:10.1063/1.3575399]

I. INTRODUCTION

The dynamics of energy transfer in atom–molecule collisions at low temperatures has garnered much attention in the context of ongoing experimental efforts to cool molecular ensembles to temperatures below 1 K through momentum-transfer collisions with atomic buffer gases.[1–3] In particular, the experimental technique of buffer-gas cooling uses cryogenic He buffer gas to produce dense ensembles of atoms or molecules at milli-Kevin temperatures[2] and generate slow molecular beams,[1,4] which can be used for trap loading, studying cold molecular collisions, and enhancing the accuracy of spectroscopic measurements.[1] The efficiency of buffer-gas cooling depends on the rate of momentum transfer and thermalization in atom–molecule collisions at low temperatures, which determine such key experimental parameters as diffusion lifetimes and rovibrational cooling rates.[1,2]

Transport phenomena in atomic and molecular gases in the absence of external fields have been the subject of many experimental and theoretical studies. Examples include measurements and calculations of transport properties of H_2 and HD in He,[12,13] CO in He,[14] I_2 in He and Ar,[16] CO_2 in He,[17] Li^+ in H_2,[15] H in He,[18,19] and O in He.[20] Hardy and coworkers calculated the diffusion coefficients of H in cold He gas and obtained quantitative agreement with experiment at temperatures below 1 K.[18] Chung and Dalgarno reported a theoretical study of diffusion of H atoms in He gas and He atoms in H gas over the temperature range 10^{-4} to 1000 K.[19] Côté *et al.* explored the possibility of creating an ultracold gas of H atoms through momentum-transfer collisions with laser-cooled alkali-metal atoms.[3] Weinstein and co-workers measured diffusion lifetimes of ground-state Ti(^2F), Ga(^2P), and In(^2P) atoms[21] and TiO($^3\Delta$) molecules[22] in ^{4}He gas at 5 K. Krems and co-workers developed a quantum scattering methodology for atom–molecule collisions in the presence of an external magnetic field[8,23] and applied the theory to calculate the rate constants for momentum transfer and spin relaxation in He + CaH and He + NH collisions.[9,10] Despite these recent developments, however, accurate quantum calculations of atom–molecule transport properties at low temperatures remain exceedingly rare.

In this work, we use rigorous quantum calculations based on an accurate *ab initio* potential energy surface (PES) to study collisional and transport properties of ground-state ThO molecules in cold ^{4}He gas. Our study is motivated by the ongoing experimental search for the electric dipole moment of the electron (EDM) with a buffer-gas-cooled beam of ThO molecules.[5,24] In this experiment, ThO molecules are first introduced in a cell filled with He or Ne buffer gas[4,5] and then allowed to expand into vacuum through a hole in the cell wall. The rotational temperature and forward velocity of the cold ThO beam thus formed depend on the timescale of diffusion and thermalization of ThO molecules in the buffer-gas cell. To assist the experimental work, we use quantum scattering

a)Electronic mail: tshcherb@cfa.harvard.edu.

theory[25–35] to calculate the cross sections and rate constants for elastic scattering, rotational relaxation, and momentum transfer in He + ThO collisions over the range of temperatures from 0.1 to 10 K. We also calculate the binding energies and equilibrium constants for the formation of the He–ThO van der Waals (vdW) complex. Formation of vdW complexes via three-body recombination with He atoms leads to trap loss[35] and may negatively impact the EDM experiment by reducing the number of free ThO molecules available for spectroscopic interrogation.

The paper is organized as follows. In Sec. II A, we present *ab initio* calculations of the He–ThO PES. Sections II B and II C describe variational calculations of bound states and chemical equilibrium coefficients for complex formation. Section III outlines the details of quantum scattering calculations of He + ThO collisions, including the effects of external electric fields. Our theoretical results for elastic scattering, momentum transfer, and inelastic relaxation in He + ThO collisions are presented in Sec. IV A and their sensitivity to the interaction potential is examined in Sec. IV C. The effects of external electric fields on collision dynamics are considered in Sec. IV B. A summary of the results follows in Sec. V.

II. HE–THO VAN DER WAALS COMPLEX

A. Potential energy surface

The interaction between ThO($X^1\Sigma^+$) and He(^{1}S) gives rise to a single adiabatic PES. To describe the geometry of the He–ThO complex, we use the standard Jacobi coordinates r, R, and θ, where r is the internuclear distance in ThO, R is the He–ThO center-of-mass separation, and θ is the angle between the vectors $\mathbf{r}$ and $\mathbf{R}$ ($\theta = 0$ corresponds to the linear He–ThO configuration). Because the vibrational frequency of ThO (896 cm^{-1}) (Ref. 36) is large compared to all other energy scales of interest in this work, we fixed the ThO internuclear distance at $r_e = 1.845$ Å, as estimated from converged calculations on the monomer[6] (the measured Born–Oppenheimer equilibrium distance[37] is slightly smaller, 1.8402 Å). The rotational constant B_e of ThO was taken as 0.332 cm^{-1}.

Previous theoretical work has established that the electronic wave function of the $X^1\Sigma^+$ state of ThO at $r \approx r_e$ can be accurately described within the scalar-relativistic single-reference coupled cluster method.[6] The same method was implemented here in its restricted version with singles, doubles, and noniterative triples [CCSD(T)] based on the standard restricted Hartree–Fock (RHF) reference.[38] We employed a small-core relativistic effective core potential ECP60MWB (Ref. 39) with the supplementary atomic natural orbital basis set[40] for the Th atom, and a correlation-consistent augmented polarized valence triple-zeta aug-cc-pVTZ basis for the O atom.[41] The O($1s^2$) and Th($5s^25p^65d^{10}$) atomic orbitals were included in the core. As shown by a detailed analysis of the monomer electric properties,[6] this basis set is not fully saturated, which may lead to underestimation of the induction and dispersion interactions within the complex. To correct this problem, we placed a set of bond functions $3s3p2d2f1g$ (Ref. 42) at the midpoint of the **R** vector. For the He atom, we used a quadruple-zeta aug-cc-pVQZ basis set.[43] The basis set superposition error was taken into account by the supermolecular approach.[44]

Ab initio calculations were performed using the MOLPRO program package[45] at 16 values of θ for 40–50 values of R from 25 Å down to the smallest R at which both the RHF and CCSD(T) procedures produced converged results. In total, 807 *ab initio* points were computed and fit to the Legendre polynomial expansion

$$V(R,\theta) = \sum_{\lambda=0}^{\lambda_{\max}} V_\lambda(R) P_\lambda(\cos\theta). \quad (1)$$

The coefficients V_λ were evaluated by fitting *ab initio* data points as follows. First, the *ab initio* points for each θ were interpolated by cubic splines to find the interaction energies at arbitrary R. Second, the angular dependence was interpolated in the same way at each R to determine the energies at $\lambda_{\max}$ Gauss–Legendre quadrature points. The coefficients V_λ were then evaluated by numerical quadrature. A 26-term expansion ($\lambda_{\max} = 25$) provided the optimal representation of the *ab initio* points with the maximum error of 1 cm^{-1} for $V < 1000$ cm^{-1} and the average root-mean-square deviation per point less than 0.01 cm^{-1}. We confirmed that the lowest-order radial coefficients with $\lambda = 0 - 3$ have the proper long-range behavior.[46]

A contour plot of the calculated He–ThO PES is shown in Fig. 1. The PES is extremely flat in the vicinity of both linear configurations ($\theta = 0$ and 180°). There is a shallow secondary minimum in the He–ThO configuration and a saddle point in the He–OTh configuration. As a result, the global minimum occurs in the bent geometry at $\theta = 157°$, $R = 4.83$ Å and it

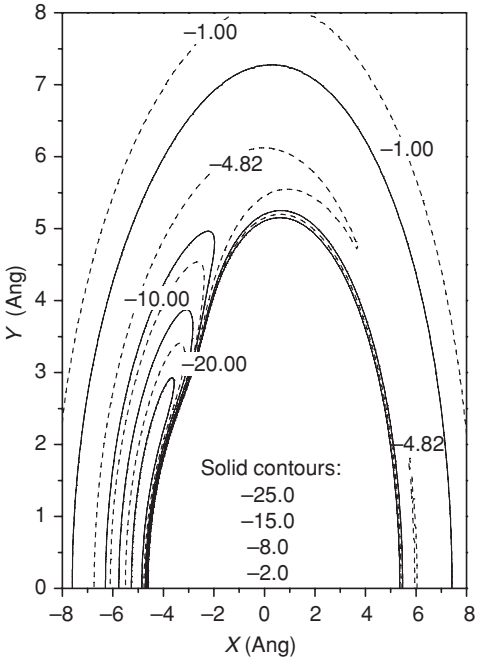

FIG. 1. Contour plot of the He–ThO PES in Cartesian coordinates $X = R\cos\theta$, $Y = R\sin\theta$. The X-axis coincides with the ThO axis. Contour energies are in cm^{-1}.

has a well depth of 28.6 cm^{-1}. A more detailed analysis[46] demonstrates that the saturation of the basis set and the correlation of the $5d^{10}$ Th shell within the CCSD(T) method may increase the binding energy by 3%, though the effect can be as large as 10% for other regions of the PES. Higher excitations in the coupled cluster method can deepen the PES, further affecting the dominant dispersion component of the interaction energy. We believe that a reliable upper bound to the He–ThO binding energy can be attained by increasing the present *ab initio* value by 20%. To reduce the computational cost of quantum scattering calculations, we choose to examine a narrower range of uncertainties ±10% in Sec. IV C.

In order to parameterize the interaction of the He–ThO collision complex with an external electric field (see Sec. III A 2 and Appendix), we have calculated the dipole moment surface (DMS) of He–ThO at the RHF level of theory. We found that the component of the DMS perpendicular to the ThO axis is negligible (<0.001 a.u.) The parallel component $d_z(r,\theta)$ was calculated on a radial grid at seven values of θ, matched to the converged CCSD(T) value of 1.153 a.u.[6] at $R = 25$ Å, and represented through an expansion in Legendre polynomials similar to that given by Eq. (1) (see Appendix).

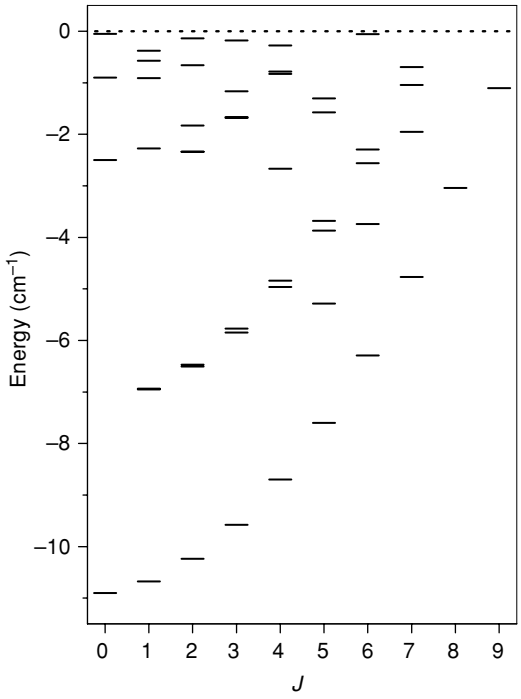

FIG. 2. Bound energy levels of the He–ThO complex. The zero of energy corresponds to the dissociation limit (dashed line).

B. Rovibrational energy levels

Throughout the paper, we consider the most abundant $^4He + {}^{232}Th^{16}O$ isotope combination. This choice also simplifies bound-state and scattering calculations, since all of the isotopes have zero nuclear spins. To calculate the rovibrational energy levels of the He–ThO complex, we used the two-dimensional Hamiltonian defined by Eq. (7) in a body-fixed coordinate frame related to vector **R** and parameterized by the total angular momentum J of the complex. Variational calculations were performed using standard basis set expansions in symmetry-adapted rigid-rotor angular functions and numerical radial functions (see, e.g., Refs. 47 and 48). For each J, separate calculations were carried out for the positive and negative parity blocks. Care was taken to locate all bound levels of the complex and ensure convergence of their energies to better than 0.05 cm^{-1}.

The energies ε_n^J of the bound levels are shown in Fig. 2. At each J, the levels are labeled by index n ($n = 0$ for the ground level), because of the strong mixing of the stretching and bending (internal rotation) motions in the He–ThO complex. The approximate assignment to stretching and bending excitations is still possible, e.g., by inspection of nodal patterns of rovibrational wave functions. In particular, the pattern in Fig. 2 reveals a very small bending frequency: the $n = 1$ and $n = 2$ levels at $J = 0$ correspond to double and quadruple bending excitations, while $n = 1$ and $n = 3$ levels at $J = 1$ correspond to single and triple excitations, since odd excitations from $J = 0$ are forbidden by parity conservation. The energy of the stretching excitation represented by the uppermost $n = 3$ level at $J = 0$ is significantly higher. Such levels do not appear as bound at higher J. The J dependence of the lowest energy levels shown in Fig. 2 is similar to that found in nonrigid linear top molecules with their characteristic l-doubling.[49] The pattern suggests that the ground vibrational state of the He–ThO complex has a collinear He–OTh configuration. The dissociation energy of the complex is 10.90 cm^{-1}, so the saddle point at $\theta = 180°$ (Fig. 1) is located well below the zero-point energy and has no effect on the ground-state complex geometry.

C. Complex-formation equilibrium

In the presence of a dense He gas, three-body collisions may lead to the formation of He–ThO vdW complexes.[35] To elucidate the possibility of He–ThO complex formation in the cold beam experiment[5] we consider the process

$$\mathrm{ThO} + \mathrm{He} \rightleftharpoons \mathrm{He} - \mathrm{ThO}. \tag{2}$$

As typical thermalization times of atomic and molecular species in cold He gas (10–100 ms) (Ref. 35) are short compared to the timescale of buffer gas cooling experiments, we can assume that the He–ThO complex is in thermal equilibrium with its constituents. The chemical equilibrium coefficient for complex formation is given by[50]

$$K = \exp\left(D_0/k_BT\right)\frac{q^{\mathrm{HeThO}}(T)}{q^{\mathrm{He}}(T)q^{\mathrm{ThO}}(T)}, \tag{3}$$

where k_B is Boltzmann's constant and T is the temperature. The first exponential factor contains the dissociation energy of the complex D_0, which reflects the energy difference between ground-state reactants and products, and q^i is the absolute partition function of species i.

Factorizing out the translational partition functions and neglecting the electronic and vibrational structure of the monomers (which is consistent with the rigid-rotor

approximation discussed above), we obtain

$$K = N_A h^3 (2\pi\mu k_B T)^{-3/2} \exp(D_0/k_B T) \frac{q_{VR}^{\mathrm{HeThO}}(T)}{q_R^{\mathrm{ThO}}(T)}, \quad (4)$$

where

$$q_{VR}^{\mathrm{HeThO}}(T) = \sum_J (2J+1) \sum_n \exp\left(-\varepsilon_n^J / k_B T\right) \quad (5)$$

and

$$q_R^{\mathrm{ThO}}(T) = \sum_j (2j+1) \exp[-B_e j(j+1)/k_B T]. \quad (6)$$

In these expressions, μ is the reduced mass of the He–ThO complex, N_A is Avogadro's number, and j is the rotational angular momentum of ThO. Equations (5) and (6) were evaluated numerically by direct counting of the energy levels. All bound levels of the complex calculated in Sec. II B were included in the summation.

Figure 3 shows that K increases rapidly with decreasing temperature. The formation of the complex will therefore reduce the number of free ThO molecules in the buffer-gas cooled beam. We note that increasing temperature not only leads K to decrease, but also causes thermal depopulation of the $j = 0$ level. A simple estimate for the fraction of free ThO($j = 0$) molecules in the beam at unit He concentration is given by $p = \{[1 + K(T)]q_R^{\mathrm{ThO}}(T)\}^{-1}$. As shown in Fig. 3, p passes through a maximum at $T = 2.5$ K, but never exceeds 15%, which suggests that He buffer gas cooling experiments[5] should be performed in the temperature range between 2 and 3 K to maximize the fraction of unclustered ThO($j = 0$) molecules in the beam.

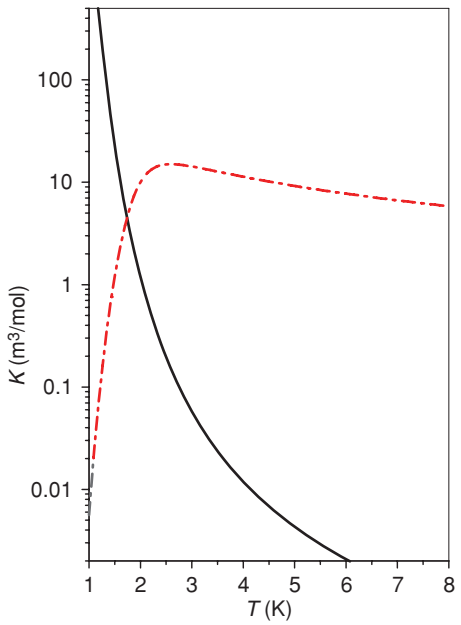

FIG. 3. Chemical equilibrium constant for the formation of the He–ThO complex (solid line) and percentage fraction of free ThO molecules p (dashed-dotted line) as functions of temperature.

III. COLLISION DYNAMICS

A. Theory

1. Field-free collisions

This section gives a brief overview of quantum scattering methodology used in this work to obtain the cross sections for elastic scattering, rotational relaxation, and momentum transfer in low-temperature He + ThO collisions. The Hamiltonian of the He–ThO collision complex may be written as ($\hbar = 1$)

$$\hat{H} = -\frac{1}{2\mu R}\frac{\partial^2}{\partial R^2} R + \frac{\hat{\mathbf{l}}^2}{2\mu R^2} + \hat{V}(\mathbf{R}, \mathbf{r}) + \hat{H}_{\mathrm{as}}, \quad (7)$$

where $\mathbf{R}$ and $\mathbf{r}$ are the Jacobi vectors introduced above, $\hat{\mathbf{l}}$ is the orbital angular momentum for the collision, and $\hat{V}(\mathbf{R}, \mathbf{r})$ is the He–ThO interaction PES calculated as described in Sec. II A. The asymptotic Hamiltonian $\hat{H}_{\mathrm{as}} = B_e \hat{\mathbf{j}}^2$, where $\hat{\mathbf{j}}$ is the rotational angular momentum of the ThO fragment.

We first consider He + ThO collisions in the absence of external fields. The wave function of the collision complex can be expanded in the form[26]

$$\Psi = \frac{1}{R} \sum_{j,l} F_{jl}^J(R) |(jl)JM\rangle, \quad (8)$$

where $\hat{\mathbf{J}} = \hat{\mathbf{j}} + \hat{\mathbf{l}}$ is the total angular momentum of the complex and

$$|(jl)JM\rangle = \sum_{m_j, m_l} (-)^{j-l+M} (2J+1)^{1/2} \times \begin{pmatrix} j & l & J \\ m_j & m_l & -M \end{pmatrix} |jm_j\rangle |lm_l\rangle \quad (9)$$

are the basis functions in the total angular momentum representation.[26] In Eq. (8), (:::) is a 3-j symbol, $|jm_j\rangle = Y_{jm_j}(\mathbf{r})$ and $|lm_l\rangle = Y_{lm_l}(\mathbf{R})$ are the spherical harmonics, which describe the orientation of collision partners in the space-fixed (SF) coordinate frame, and $M = m_j + m_l$ is the projection of J on the SF quantization axis. Substitution of Eq. (8) into the Schrödinger equation with Hamiltonian (7) yields the standard system of close-coupled (CC) equations in the total angular momentum representation[25,26]

$$\left[\frac{d^2}{dR^2} - \frac{l(l+1)}{R^2} + k_j^2\right] F_{jl}^J(R) = 2\mu \sum_{j',l'} \langle (jl)JM|\hat{V}(R,\theta)|(j'l')JM\rangle F_{j'l'}^J(R), \quad (10)$$

where $k_j^2 = 2\mu E_C = 2\mu(E - \epsilon_j)$ is the wave vector for the incident collision channel with energy ϵ_j, E_C is the collision energy, and E is the total energy. The matrix elements of the interaction potential on the right-hand side of Eq. (10) can be evaluated analytically as described elsewhere[25,26] in terms of the radial expansion coefficients $V_\lambda(R)$ of the interaction potential (1).

Collisional and transport properties of a molecule in a buffer gas are determined by the generalized integral cross

sections $\sigma^{(n)}_{j\to j'}(E_C)$[14,17,51]

$$\sigma^{(0)}_{j\to j'}(E_C) = 2\pi \int \sin\theta d\theta \frac{d\sigma_{j\to j'}}{d\Omega}(\theta, E_C) = \frac{\pi}{k_j^2(2j+1)} \sum_J (2J+1) \sum_{l,l'} \left|T^J_{jl;j'l'}\right|^2 \quad (11)$$

and

$$\sigma^{(1)}_{j\to j'}(E_C) = 2\pi \int \sin\theta d\theta \frac{d\sigma_{j\to j'}}{d\Omega}(\theta, E_C) \left[1 - \left(\frac{k_{j'}}{k_j}\right)\cos\theta\right], \quad (12)$$

where $n = 0$ corresponds to the conventional integral cross section and $n = 1$ to the momentum transfer cross section.[15,17–19,23] In these expressions, $\frac{d\sigma_{j\to j'}}{d\Omega}(\theta, E_C)$ is the differential cross section (DCS) defined by

$$\frac{d\sigma_{j\to j'}}{d\Omega}(\theta, E_C) = \frac{1}{k_j^2(2j+1)} \sum_{m_j, m'_j} \left|q_{jm_j\to j'm'_j}(\theta, E_C)\right|^2, \quad (13)$$

where

$$q_{jm_j\to j'm'_j}(\theta, E_C) = \sqrt{\pi} \sum_l \sum_{l', m'_l} \mathrm{i}^{l-l'} [(2l+1)]^{1/2} \times \frac{1}{\sqrt{2\pi}} \Theta_{l'm'_l}(\theta) \sum_{J,M} (-)^{l+l'+j+j'} (2J+1) \times \begin{pmatrix} j & l & J \\ m_j & 0 & -M \end{pmatrix} \begin{pmatrix} j' & l' & J \\ m'_j & m'_l & -M \end{pmatrix} T^J_{jl;j'l'} \quad (14)$$

is the scattering amplitude, $\Theta_{l'm'_l}(\theta)$ is the normalized associated Legendre polynomial as defined by Zare,[27] and $T^J_{jl;j'l'}$ are the T-matrix elements, which can be obtained from the solution of the CC equations (10). Equation (14) can be obtained from Eq. (12) of Ref. 28 by taking the quantization axis of the incident collision flux to coincide with the initial relative velocity vector ($\Theta = \Phi = 0$). Thermal averaging of the generalized cross sections given by Eqs. (11) and (12) yields state-to-state rate constants for inelastic relaxation ($n = 0$) and momentum transfer ($n = 1$)

$$k^{(n)}_{j\to j'} = \left(\frac{8\pi\mu}{k_BT}\right)^{1/2} \frac{1}{(k_BT)^{3/2}} \int dE_C E_C e^{-E_C/k_BT} \sigma^{(n)}(E_C). \quad (15)$$

The first-order Chapman–Enskog theory of transport phenomena[51] gives the following expression for the binary diffusion coefficient of a molecule diffusing through an atomic buffer gas[14,15,17–19]

$$D = \frac{3k_BT}{16n\mu} [\Omega^{(1,1)}]^{-1}, \quad (16)$$

where n is the He number density, and $\Omega^{(1,1)}$ is the collision integral[14,17]

$$\Omega^{(1,1)} = \left(\frac{1}{8\pi\mu}\right)^{1/2} \frac{1}{(k_BT)^{5/2}} \int dE_C E_C^2 e^{-E_C/k_BT} \sigma^{(1)}(E_C, T). \quad (17)$$

The quantity $\sigma^{(1)}(E_C, T)$ is related to the generalized momentum-transfer cross sections (12) as

$$\sigma^{(1)}(E_C, T) = \sum_{j,j'} w_j(T) \sigma^{(1)}_{j\to j'}(E_C), \quad (18)$$

where $w_j(T) = [q_R^{\mathrm{ThO}}]^{-1}(2j+1)e^{-\epsilon_j/k_BT}$ are the Boltzmann weights and q_R^{ThO} is the rotational partition function given by Eq. (6). We note that $\sigma^{(1)}(E_C, T)$ depends on *both* the temperature and collision energy.

It is convenient to define the effective diffusion cross section[11,18]

$$\sigma_D = \Omega^{(1,1)} \left(\frac{2\pi\mu}{k_BT}\right)^{1/2}. \quad (19)$$

In the following, we will use σ_D rather than the density-dependent diffusion coefficient (16) to characterize the transport properties of ThO in He. If necessary, D can be obtained from σ_D for any given n using Eqs. (16) and (19).

We integrated the CC equations (10) numerically using the log-derivative algorithm[52] on a radial grid from $R_{\min} = 4\,a_0$ to $R_{\max} = 40\,a_0$ with a grid step of $0.04\,a_0$. A total of 18 rotational states of ThO ($j = 0 - 17$) were included in the basis set expansion (8) and scattering calculations were carried out for 26 values of the total angular momentum ($J = 0 - 25$). The angular integral in Eq. (12) was evaluated on a 30-point Gauss–Legendre quadrature. The calculated integral and momentum-transfer cross sections were converged to within 5%. The collision integral (15) was evaluated using the trapezoidal rule on a grid of 2699 collision energies from $E_C = 0.01$ to 25 cm^{-1}. The summation in Eq. (18) included eight lowest rotational states of ThO, and the calculated diffusion cross sections were converged to <5% in the temperature range between 0.1 and 10 K.

2. Collisions in the presence of a dc electric field

In the presence of an external dc electric field, the asymptotic Hamiltonian in Eq. (7) takes the form

$$\hat{H}_{\mathrm{as}} = B_e\hat{\mathbf{j}}^2 - \mathbf{E}\cdot[\mathbf{d}_0 + \mathbf{d}(R,\theta)], \quad (20)$$

where $\mathbf{E}$ is the electric field vector, $\mathbf{d}_0$ is the permanent dipole moment of the ThO monomer, and $\mathbf{d}(R,\theta)$ accounts for the variation of $\mathbf{d}_0$ induced by the interaction with the He atom. In the asymptotic approximation (see Appendix), the term $\mathbf{d}(R,\theta)$ is neglected, and Eq. (20) reduces to

$$\hat{H}_{\mathrm{as}} = B_e\hat{\mathbf{j}}^2 - \mathbf{E}\cdot\mathbf{d}_0. \quad (21)$$

In Appendix, we show that the term $\mathbf{d}(R,\theta)$ has a minor influence on cold He + ThO collisions for electric fields below 100 kV/cm.

The total angular momentum of the collision complex is not conserved in the presence of an electric field, and we expand the wave function in direct products of spherical harmonics[7,8,23]

$$\Psi = \frac{1}{R} \sum_{j,m_j} \sum_{l,m_l} F^M_{jm_jlm_l}(R) |jm_j\rangle |lm_l\rangle. \quad (22)$$

The radial expansion coefficients are now labeled by the total angular momentum projection M, which is conserved for

collisions in an electric field. The system of CC equations in the uncoupled SF representation takes the form

$$\left[\frac{d^2}{dR^2} - \frac{l(l+1)}{R^2} + 2\mu E\right] F^M_{jm_j lm_l}(R) = 2\mu \sum_{j'm'_j} \sum_{l'm'_l} \langle jm_j|\langle lm_l|\hat{V}(R,\theta) + \hat{H}_{\rm as}|j'm'_j\rangle|l'm'_l\rangle F^M_{j'm'_j l'm'_l}(R). \quad (23)$$

The matrix elements of the interaction potential on the right-hand side can be evaluated analytically[8] in terms of the V_λ coefficients defined by Eq. (1). Unlike in the case of zero electric field, the matrix elements of the asymptotic Hamiltonian $\hat{H}_{\rm as}$ are not diagonal in the limit $R \to \infty$ because electric fields induce couplings between different rotational states.[32] It is therefore necessary to transform the wave function to the asymptotic representation in which $\hat{H}_{\rm as}$ is diagonal.[8,23] After applying the transformation, the radial expansion coefficients can be matched to the standard asymptotic form[8,23] to yield the T-matrix elements in the uncoupled representation $T_{jm_j lm_l;j'm'_j l'm'_l}$. The integral cross sections for transitions between different Stark levels are given by[23,29]

$$\sigma_{jm_j \to j'm'_j}(E_C) = \frac{\pi}{k^2_{jm_j}} \sum_{l,m_l} \sum_{l',m'_l} |T_{jm_j lm_l;j'm'_j l'm'_l}|^2. \quad (24)$$

We emphasize that scattering calculations in the uncoupled representation (22) are computationally demanding due to nonconservation of the total angular momentum, which results in a rapid growth in the number of scattering channels with increasing rotational basis set size. To reduce computational cost, we used moderate-size basis sets, which included 13 rotational states ($j = 0 - 12$) and 14 partial waves ($l = 0 - 13$), leading to 1638 scattering channels for $M = 0$. Because of the limited number of partial waves in the basis, we were able to obtain converged results only at collision energies below 2 cm^{-1}. We note that this limitation does not apply to field-free collisions, where the use of the total angular momentum representation (9) allows for efficient scattering calculations with large rotational basis sets and high collision energies.[30]

IV. RESULTS

A. Field-free collisions

In this section, we present the results for elastic scattering, rotationally inelastic transitions, and momentum transfer in He + ThO collisions in the absence of an electric field.

Figure 4 shows the integral cross sections for elastic scattering and rotational energy transfer in He + ThO collisions. A complicated resonance structure is apparent in the energy dependence of both the elastic and inelastic cross sections. The resonances arise due to the anisotropy of the interaction potential, which couples the incident collision channel with closed rotationally excited channels. The resonance structure has been observed previously in quantum calculations of He + CO and He + HCN collisions at low collision energies.[14,53] The structure is most pronounced for low initial j. For $j > 1$, the resonances show up as peaks on top

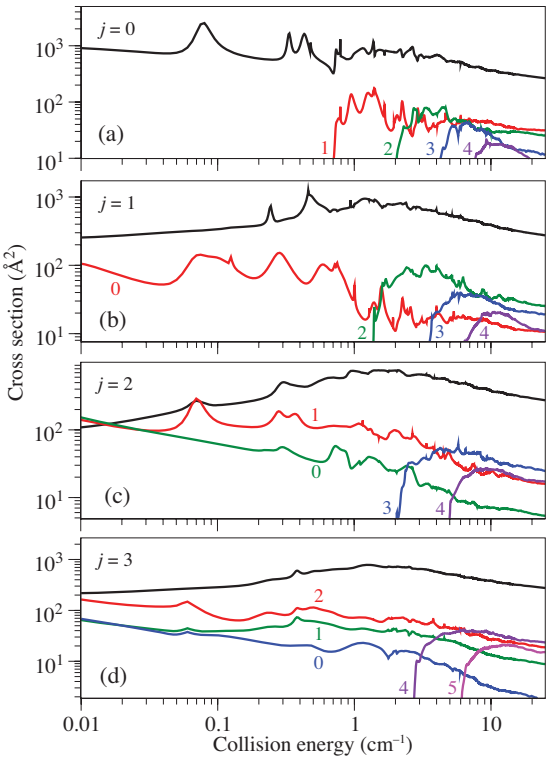

FIG. 4. State-resolved integral cross sections $\sigma^{(0)}_{j\to j'}$ for $j = 0$ (a), 1 (b), 2 (c), and 3 (d) plotted vs collision energy in the absence of an electric field. The curves are labeled by the values of j'.

of a smoothly varying background, with gradually diminishing peak heights with increasing collision energy. The cross sections for rotational excitation near threshold follow the dependence $\sigma_{j\to j'}(E_C) \propto (E_C - \epsilon'_j)^{1/2}$ where $\epsilon_{j'}$ is the threshold energy.

The energy dependence of total elastic and inelastic cross sections is displayed in Fig. 5. The total inelastic cross sections are obtained by summing the state-resolved integral cross sections (11) over all energetically accessible final rotational states. At collision energies below 1 cm^{-1}, when only a few rotational channels are open, the energy dependence of both the elastic and inelastic cross sections is dominated by broad resonances, which are especially pronounced for $j = 0$. The inelastic cross section for the $j = 1$ initial channel features a deep minimum near $E_C \sim 1$ cm^{-1}. At higher collision energies, many rotational transitions contribute to the total elastic and inelastic cross sections, and their absolute magnitudes become independent of the initial rotational state. This effect is clearly observed in Fig. 5: the curves corresponding to different initial j tend to the same asymptotic limit with increasing E_C, and are within 10% of each other at $E_C > 10$ cm^{-1}.

The cross sections for elastic scattering and momentum transfer are compared in Fig. 6 as functions of collision energy. We observe that (1) the cross sections for momentum transfer are generally smaller than their elastic counterparts at high collision energies; (2) the difference between the two types of cross sections increases with collision energy; and (3) at very low collision energies approaching the Wigner threshold regime, the two cross sections become identical,

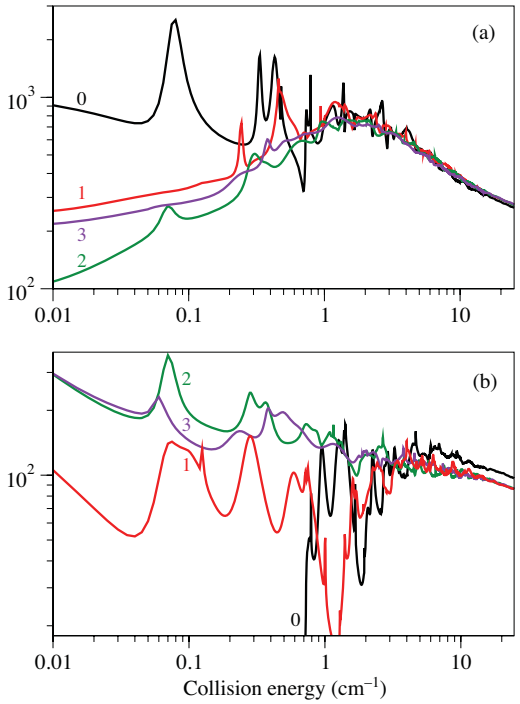

FIG. 5. Initial state-resolved elastic (a) and inelastic (b) integral cross sections $\sigma_j^{(0)} = \sum_{j'} \sigma_{j\to j'}^{(0)}$ plotted vs collision energy for different j and zero electric field.

with the momentum transfer cross section being *larger* than the elastic cross section.

Figure 7 presents a similar comparison for rotationally inelastic cross sections. The energy dependence of the cross

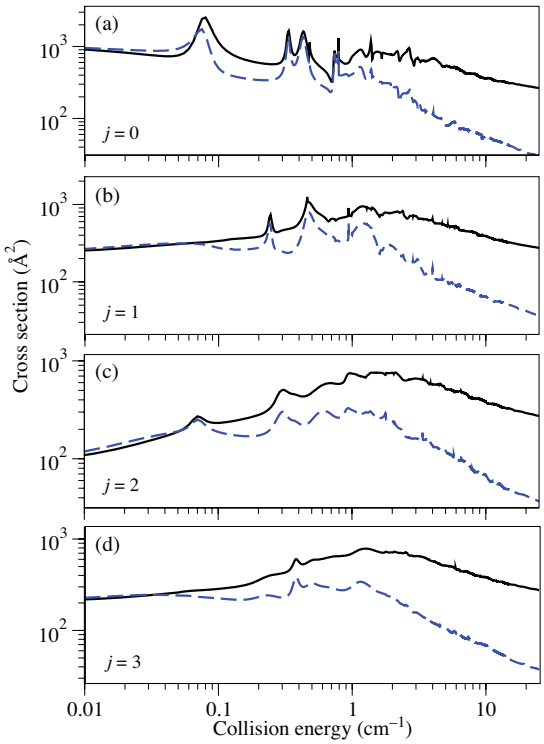

FIG. 6. Cross sections for elastic scattering $\sigma_{j\to j}^{(0)}$ (full lines) and momentum transfer $\sigma_{j\to j}^{(1)}$ (dashed lines) plotted vs collision energy for $j = 0$ (a), 1 (b), 2 (c), and 3 (d).

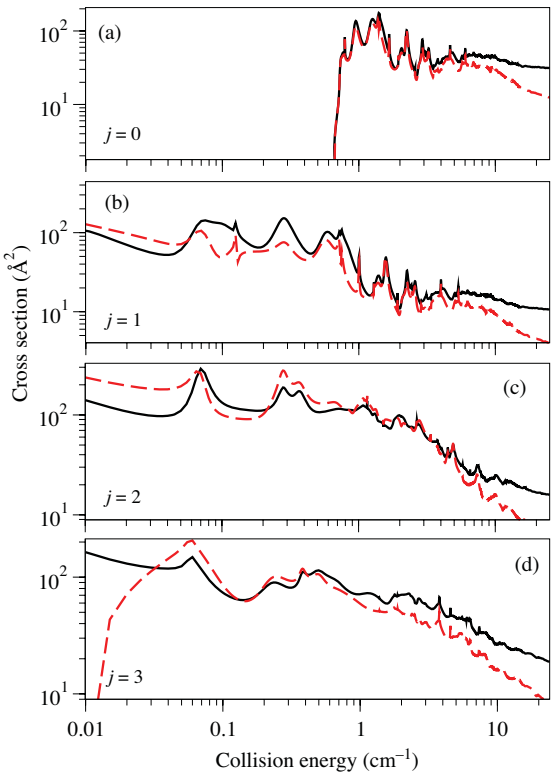

FIG. 7. Cross sections for rotational relaxation $\sigma_{j\to j-1}^{(0)}$ (full lines) and momentum transfer $\sigma_{j\to j-1}^{(1)}$ (dashed lines) vs collision energy for $j = 1$ (b), 2 (c), and 3 (d). Panel (a) shows the cross sections for rotational excitation $\sigma_{0\to 1}^{(0)}$ (full line) and $\sigma_{0\to 1}^{(1)}$ (dashed line).

sections in panel (a) is qualitatively similar to that shown in Fig. 6: the cross sections for momentum transfer accompanied by rotational excitation approach their integral counterparts in the threshold regime ($E_C \sim \epsilon'_j$), and become smaller at higher collision energies. The situation for rotational relaxation cross sections is markedly different and varies dramatically from one transition to another. At low collision energies ($E_C < 0.1$ cm^{-1}), the momentum transfer cross sections for the $j = 1 \to 0$ and $j = 2 \to 1$ transitions are larger than the integral cross sections. At intermediate collision energies ($0.1 < E_C < 5.0$ cm^{-1}), both kinds of cross sections become comparable to each other, and at $E_C > 1$ cm^{-1}, the integral cross section is larger in magnitude. In contrast, the momentum transfer cross section for the $j = 3 \to 2$ transition begins to decline dramatically below $E_C = 0.05$ cm^{-1}, and takes a negative value at $E_C = 0.01$ cm^{-1} (in actual calculations, the negative values were replaced by zeros).

To rationalize the unusual behavior of momentum transfer cross sections shown in Fig. 7(d), let us consider the definition (12). The ratio of the relative velocities in the outgoing and incoming collision channels $k_{j'}/k_j$ multiplying $\cos\theta$ in Eq. (12) can be recast in the form[17]

$$\frac{k_{j'}}{k_j} = \left[1 + \frac{\Delta\epsilon_{jj'}}{E_C}\right]^{1/2}. \tag{25}$$

When the collision energy is small compared to the energy separation between the initial and final rotational states ($E_C \ll \Delta\epsilon_{jj'}$), we have $k_{j'}/k_j \gg 1$. If the differential cross

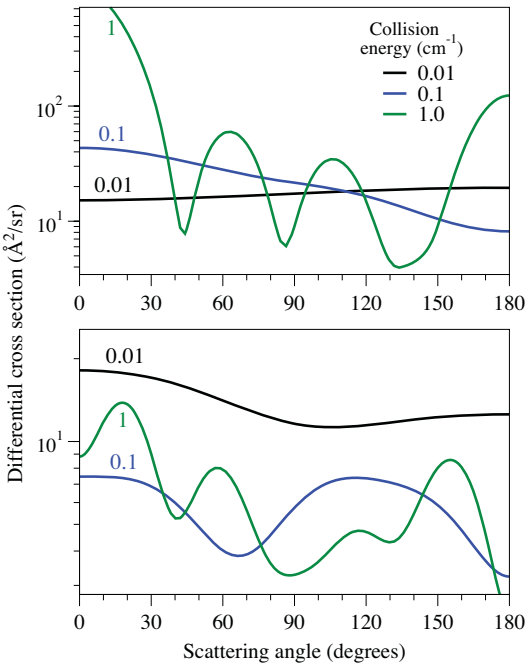

FIG. 8. (Upper panel) Elastic DCS vs scattering angle θ for $E_C = 0.01, 0.1$, and 1 cm^{-1}. Note the strongly pronounced forward peak at $E_C = 1$ cm^{-1}. (Lower panel) Inelastic DCS for the $j = 3 \rightarrow 2$ transition vs scattering angle calculated for the same collision energies as in the upper panel.

section is peaked in the backward direction ($\cos\theta \sim 1$), the term $(k_{j'}/k_j)\cos\theta$ in Eq. (12) becomes large and outweighs the first term, thereby reducing the cross section for momentum transfer.

To illustrate this point, we plot in Fig. 8 the angular dependence of elastic and inelastic DCSs at three selected collision energies. At the lowest collision energy of $E_C = 0.01$ cm^{-1}, the DCSs vary slowly with θ because only the first few l terms in the partial wave expansion of the scattering amplitude (14) are different from zero. A larger number of partial waves contributes at higher collision energies (0.1 and 1.0 cm^{-1}), causing the elastic DCS to become increasingly more forward-peaked. By definition (12), the cross sections for momentum transfer are not sensitive to the amplitude of the DCS in the forward-scattering region, where $\cos\theta \sim 0$. As a result, the cross sections decline more rapidly with collision energy as shown in Fig. 6. This behavior was observed previously for Li + H collisions at low temperatures.[3] In contrast, the inelastic DCSs shown in the lower panel of Fig. 8 do not become more forward-peaked with increasing collision energy. In particular, the DCS for the $j = 3 \rightarrow 2$ transition has a non-negligible amplitude in the backward direction where $\cos\theta \sim 1$, which explains the small magnitude of the inelastic momentum transfer cross sections and their rapid decline with E_C shown in Fig. 7(d).

We emphasize that the abrupt decline of momentum transfer cross sections only occurs for inelastic collisions at low temperatures. It is only under these conditions that the term proportional to $\cos\theta$ in Eq. (12) can become larger than 1. In the case of elastic collisions $k_{j'}/k_j = 1$ and the cross sections for momentum transfer are well-behaved at low collision energies. We therefore limit our consideration of transport properties of ThO in He to temperatures between 0.1 and 10 K, where elastic scattering dominates and diffusion cross sections (19) are unaffected by the anomalous behavior.

Table I lists state-to-state rate constants for inelastic relaxation and momentum transfer in He + ThO collisions at 4 K. The rate constants for momentum transfer are smaller than those for elastic scattering for all j. The inelastic transitions changing j by 1 or 2 are the most efficient. At low initial j, the rate constants $k^{(0)}_{j\rightarrow j'}$ and $k^{(1)}_{j\rightarrow j'}$ are very close to each other (except when $j = j'$). As j increases, however, the rate constants for inelastic momentum transfer become much smaller than those for inelastic relaxation. This is another manifestation of the anomalous behavior discussed above and shown in Fig. 7(d). The energy difference $\Delta\epsilon_{jj'}$ increases linearly with j, so the abrupt decline of momentum-transfer cross sections shown in Fig. 7(d) shifts to higher E_C with increasing j, affecting the rate constants for momentum transfer at 4 K. This observation suggests that the suppression of momentum transfer in inelastic collisions might be observed experimentally by measuring thermalization dynamics of rotationally excited ThO in a 4 K buffer gas cell.

Figure 9 shows the effective diffusion cross section (19) for ThO in ^{4}He as a function of temperature. The monotonous decline of the cross section mirrors that of j-resolved momentum transfer cross sections plotted in Fig. 5. Our calculated diffusion cross section decreases from 561.0 Å^2 to 86.7 Å^2 as temperature increases from 0.1 to 10 K. Skoff *et al.* have recently measured the diffusion cross section of YbF($^2\Sigma$) molecules in ^{4}He gas to be 161 ± 49 Å^2 at 20 K.[11] It would be interesting to extend our calculations to higher temperatures to see if the monotonous, featureless decline of the diffusion cross section shown in Fig. 9 persists at higher temperatures. We did not pursue this in the present work because of the large number of rotational transitions that contribute to Eq. (15) and slow convergence of the angular integrals in Eq. (12) arising due to the highly oscillatory angular dependence of the DCS at high collision energies.

B. Collisions in an electric field: *j*-changing and m_j-changing transitions

Figure 10 shows the Stark shifts of ThO versus the applied electric field. By applying an electric field of 150 kV/cm, the $j = 0$ rotationally ground state can be shifted by 5 cm^{-1}. We consider collisions of ThO molecules initially in the $|jm_j\rangle = |10\rangle$ Stark state, which is low-field-seeking for electric fields below ~50 kV/cm. Collisions with He atoms induce rotational relaxation to the ground Stark level $|10\rangle \rightarrow |00\rangle$, along with j-conserving, but m_j-changing transitions $|10\rangle \rightarrow |1, \pm1\rangle$. The Stark levels $|11\rangle$ and $|1, -1\rangle$ are degenerate, and the cross section for the $|10\rangle \rightarrow |11\rangle$ transition is the same as that for the $|10\rangle \rightarrow |1, -1\rangle$ transition. The j-changing and m_j-changing transitions are marked by red arrows in Fig. 10. We carry out scattering calculations for $E = 0$, 50, 100, and 150 kV/cm, and obtain the cross sections for elastic, m_j-changing, and rotational relaxation in the collision energy interval 0.01–2 cm^{-1}.

Figure 11 shows the cross sections for elastic scattering and j-changing and m_j-changing Stark relaxation as

TABLE I. Rate constants for rotationally inelastic scattering ($k^{(0)}_{j\to j'}$) and momentum transfer ($k^{(1)}_{j\to j'}$) in He + ThO collisions at $T = 4$ K calculated for zero electric field. The rate constants are given in units of 10^{-11} cm^3/s.

j	j'	$k^{(0)}_{j\to j'}$	$k^{(1)}_{j\to j'}$	j	j'	$k^{(0)}_{j\to j'}$	$k^{(1)}_{j\to j'}$
0	0	83.73	22.30	4	0	0.71	0.42
	1	6.93	5.49		1	2.18	1.38
	2	5.74	5.18		2	4.24	2.69
	3	2.30	2.17		3	7.01	4.55
	4	0.58	0.51		4	78.58	19.26
	5	0.16	0.14		5	2.66	2.08
	6	0.03	0.02		6	0.47	0.40
1	0	2.93	2.14	5	0	0.52	0.25
	1	83.68	22.85		1	1.37	0.66
	2	7.73	7.32		2	2.41	1.39
	3	2.79	2.54		3	4.28	2.54
	4	0.76	0.66		4	7.18	4.10
	5	0.18	0.15		5	76.69	18.38
	6	0.04	0.03		6	2.22	1.68
2	0	2.35	1.94	6	0	0.31	0.17
	1	7.48	7.14		1	1.08	0.60
	2	79.33	20.70		2	1.77	0.88
	3	4.88	3.93		3	2.54	1.24
	4	1.43	1.21		4	4.52	2.04
	5	0.30	0.26		5	7.87	3.43
	6	0.06	0.06		6	72.45	16.90
3	0	1.38	1.16	7	0	0.18	0.10
	1	3.95	3.22		1	0.68	0.38
	2	7.14	5.03		2	1.44	0.69
	3	78.64	19.99		3	2.05	0.70
	4	3.46	2.73		4	2.67	0.79
	5	0.78	0.67		5	4.97	1.53
	6	0.13	0.11		6	8.73	2.84

functions of collision energy for several values of the electric field.[29] While the elastic cross section does not exhibit strong variations with the field, the energy dependence of the inelastic cross sections is strongly modified as the field is varied from zero to 50 kV/cm. This effect resembles the electric field enhancement of Stark relaxation in cold

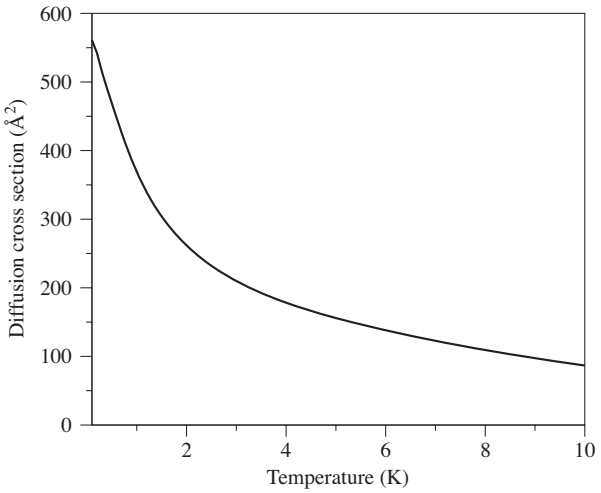

FIG. 9. Diffusion cross section (19) for ThO in He as a function of temperature.

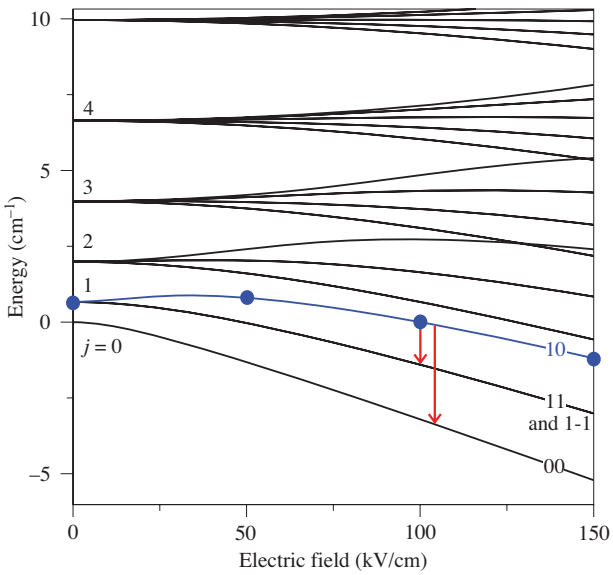

FIG. 10. Stark shifts of ThO($X^1\Sigma^+_g$) vs electric field. The points represent the electric field values at which scattering calculations were performed. The arrows show the inelastic transitions considered in this work.

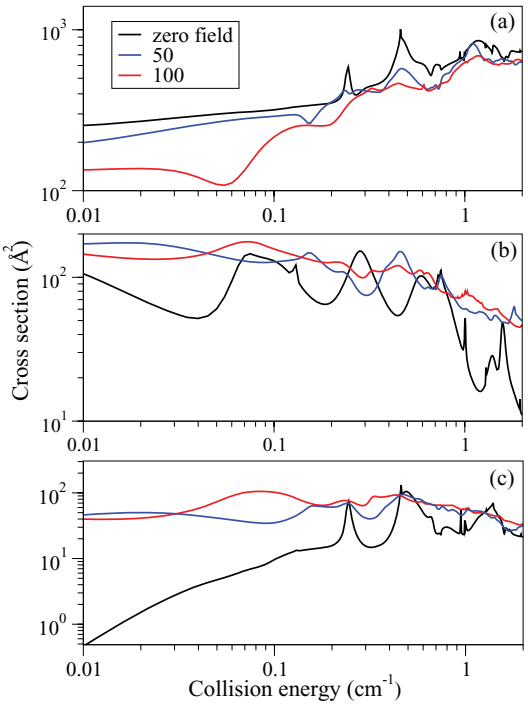

FIG. 11. Cross sections for elastic scattering (a) and Stark relaxation via the transitions $|10\rangle \rightarrow |00\rangle$ (b) and $|10\rangle \rightarrow |11\rangle$ (c) vs collision energy calculated for $E = 0$, 50, and 100 kV/cm (see color legend).

He + OH collisions,[31] and can be explained as follows. In the absence of an electric field, the cross sections at collision energies below 1 cm^{-1} are dominated by narrow shape resonances, which can be viewed as metastable states of the atom–molecule collision complex with orbital angular momentum l trapped by centrifugal barriers in incoming and/or outgoing collision channels. An external electric field couples different rotational states of the polar molecule within the complex, which leads to additional couplings between different l induced by the anisotropic part of the interaction potential.[32] These couplings reduce the lifetime of the metastable states, leading to the field-induced broadening of narrow resonance features shown in Fig. 11.

Table II illustrates the effect of electric fields on inelastic relaxation rates. The rate constants for both j-changing and m_j-changing transitions increase monotonously with the field strength below $E = 100$ kV/cm. The enhancement is particularly strong for the j-conserving, m_j-changing transition $|10\rangle \rightarrow |11\rangle$ at $T = 0.1$ K. This is because the cross section for this transition tends to zero with decreasing collision energy in the absence of an electric field as shown in Fig. 11(c). Because the total angular momentum projection $M = m_j + m_l$ is conserved, m_j-changing transitions must be accompanied by a change in m_l. As a result, there is a centrifugal barrier in the outgoing collision channel, which suppresses m_j-changing collisions at zero field. The degeneracy of different m_j states is removed by an external electric field, so the m_j-changing transitions can occur without impediment once the field-induced splitting between the m_j states is large compared to the barrier height.

TABLE II. Rate constants for collision-induced Stark relaxation from the $|j = 1, m_j = 0\rangle$ level of ThO (see Fig. 10) calculated for $T = 0.1$ and 1 K and different electric fields (in kV/cm). The rate constants are given in units of 10^{-11} cm^3/s.

Temperature	Electric field	$\|10\rangle \rightarrow \|00\rangle$	$\|10\rangle \rightarrow \|11\rangle$
0.1	0	2.21	0.31
	50	2.96	1.11
	100	3.25	1.82
	150	2.93	1.30
1.0	0	3.05	2.15
	50	4.41	3.01
	100	4.68	3.38
	150	4.43	3.03

C. Sensitivity to the interaction potential

Quantum scattering calculations reported in the previous sections yield exact results for a given PES. At low temperatures, however, these results become sensitive to small variations in the interaction PES, which are beyond the accuracy of modern *ab initio* methods. It is therefore desirable to examine the variation of scattering observables to small changes in the He–ThO interaction potential. To this aim, we repeated the scattering calculations with the interaction potential multiplied by a constant scaling factor f_s. Figure 12 shows the variation of the integral and transport cross sections with collision energy calculated for five equally spaced values of f_s in the range 0.90–1.10. These values are chosen based on test *ab initio* calculations presented in Sec. II A. We observe that the resonance structure at low collision energies is extremely sensitive to small variations of the interaction potential. The resonance positions and widths change dramatically with increasing f_s, as expected for a collision process dominated by the few lowest partial waves.[54,55] More specifically, the magnitude of the scattering cross sections in this regime is determined by the existence of quasibound states of the He–ThO complex and their proximity to the collision threshold. At higher collision energies, the system enters the multiple-partial-wave regime, the resonance structure gets

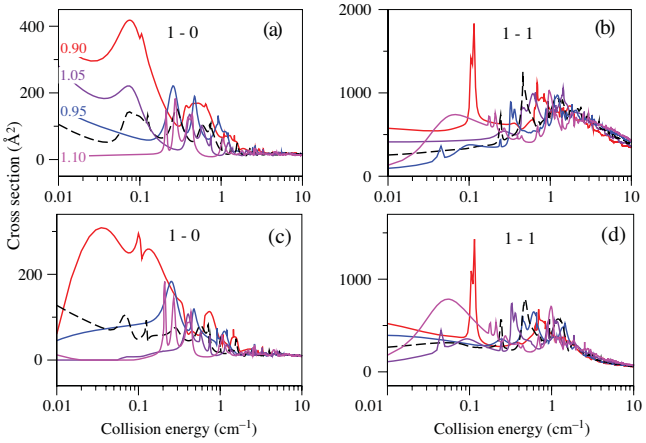

FIG. 12. Integral (a, b) and momentum-transfer (c, d) cross sections for the $j = 1 \rightarrow 0$ (a, c) and $j = 1 \rightarrow 1$ (b, d) transitions as functions of collision energy calculated for different values of the scaling parameter f_s indicated in panel (a). The cross sections for unmodified PES ($f_s = 1$) are shown by dashed lines.

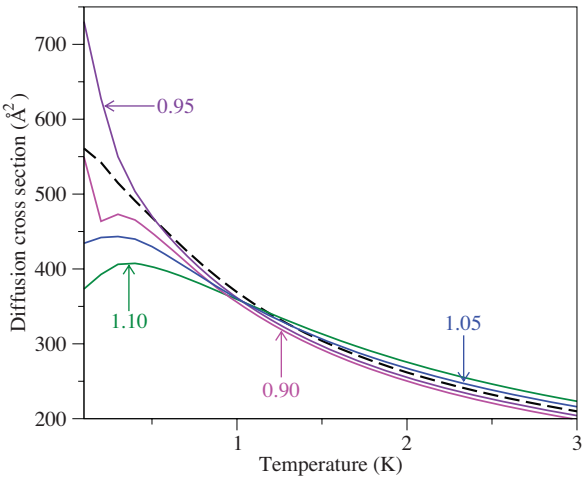

FIG. 13. Diffusion cross sections (19) for ThO in He as functions of temperature calculated for different values of the scaling parameter f_s. The results obtained for $f_s = 1$ are shown by the dashed line.

washed out (see Sec. III B) and the cross sections become insensitive to f_s.

Figure 13 shows the temperature dependence of He–ThO diffusion cross sections calculated for different values of f_s. In contrast to the situation shown in Fig. 13, the diffusion cross sections are almost unaffected by scaling the PES, except at very low temperatures (<1 K). We attribute this remarkable lack of sensitivity to the fact that σ_D defined by Eq. (19) contains contributions from transitions between many initial and final rotational states of ThO. So even though the individual terms in Eq. (19) may be very sensitive to the interaction potential, their thermally averaged linear combination is not. We estimate the accuracy of our calculated He–ThO diffusion cross sections to be within 10% for temperatures above 1 K.

V. SUMMARY

We have presented an accurate *ab initio* interaction PES of the He–ThO complex calculated using the CCSD(T) method and extended basis sets with effective core potentials that account for scalar relativistic effects. We found that the global minimum of the PES corresponds to the bent geometry and is 28.6 cm^{-1} deep. Using variational calculations of rovibrational energy levels, we estimated the dissociation energy of the complex to be 10.9 cm^{-1}.

The calculated energy levels have been used to evaluate the chemical equilibrium constant for the formation of the He–ThO vdW complex as a function of temperature. We have shown that complex formation is thermodynamically favored at low temperatures and may cause significant loss of free ThO molecules below 1 K. Our calculations demonstrate that the abundance of free ground-state ThO molecules reaches a maximum in the temperature interval of 2–3 K.

Rigorous quantum calculations based on the *ab initio* PES computed in this work demonstrate that rotational relaxation in cold He + ThO collisions is very efficient at collision energies below 1 cm^{-1}, where the cross sections display a rich resonance structure. At high collision energies ($E_C > 10$ cm^{-1}) both the elastic and inelastic cross sections decline monotonously with collision energy, and are insensitive to the initial rotational state of ThO (Fig. 5). The cross sections for momentum transfer become identical to the integral cross sections in the limit of vanishing collision energy (Fig. 6). At higher collision energies, the momentum transfer cross sections are smaller and decrease faster with collision energy than do the integral cross sections. These findings can be rationalized based on the angular dependence of the elastic DCS shown in Fig. 8, which peaks strongly in the forward direction at high collision energies, but becomes isotropic in the *s*-wave threshold regime.

The variation of the inelastic cross sections for momentum transfer with collision energy is more complicated (Fig. 7): at high collision energies, these cross sections follow the same tendency as the elastic cross sections. However, when the collision energy is small and the energy difference between the initial and final rotational channels is large, the inelastic momentum transfer cross sections can decrease abruptly to zero or even become negative (Fig. 7). Because the cross sections cannot be negative, the sign change is unphysical and might indicate a breakdown of the Chapman–Enskog theory of transport phenomena, which is based on a classical description of translational degrees of freedom.[33] The suppression of inelastic momentum transfer in collisions of rotationally excited ThO molecules with He atoms that precedes the sign change [Fig. 7(d)] might, however, have some physical meaning. If so, this suppression should be observable in experiments on rotational thermalization of ThO molecules in He at 4 K. Measurements of other transport properties such as viscosity and thermal conductivity of rotationally excited ThO molecules in cold He gas would be instructive.

In order to assist the ongoing experimental work[5,11,24] on the preparation and characterization of cold beams of polar molecules, we calculated the temperature dependence of the diffusion cross section for ThO in He gas. We find that the cross section is a monotonously decreasing function of temperature (Fig. 11). The magnitude of the calculated cross section is consistent with a recent experimental measurement of YbF diffusion in He gas at 20 K.[11] Both the integral and momentum-transfer cross sections are sensitive to small variations of the PES at low collision energies (Fig. 12), but become more robust against these variations at higher collision energies. The diffusion cross sections are far less sensitive to inaccuracies in the PES because of the thermal and rotational-state averaging in Eq. (19). At temperatures above 1 K, our calculated diffusion cross sections are accurate to within 10% (Fig. 13).

We have examined the effects of an external electric field on j-changing and m_j-changing transitions in cold He + ThO collisions. We found that the cross sections for both type of transitions are sensitive to the magnitude of the external field. In particular, the rate constant for the $|10\rangle \rightarrow |00\rangle$ transition increases by a factor of 1.4 at $T = 1$ K and by a factor of 3.6 at $T = 0.1$ K as the electric field is varied from 0 to 50 kV/cm (Fig. 11 and Table I). These results indicate that rotational depolarization in low-temperature collisions of $^1\Sigma$-state molecules with $^1S_0$-state atoms can be stimulated with electric fields.

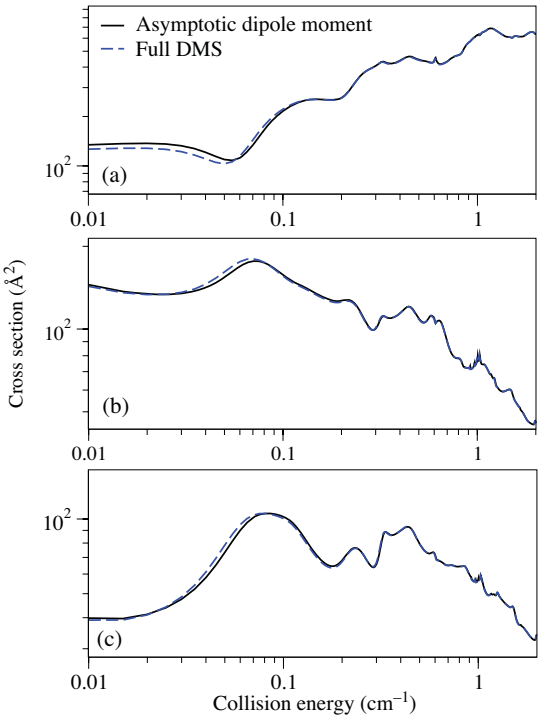

FIG. 14. Cross sections for elastic scattering (a) and Stark relaxation via the transitions $|10\rangle \rightarrow |00\rangle$ (b) and $|10\rangle \rightarrow |11\rangle$ (c) vs collision energy. Full line: calculations using the asymptotic approximation for the dipole moment, dashed line: calculations using the *ab initio* DMS of He–ThO. The electric field is 100 kV/cm.

As shown in Fig. 14, the cross sections for elastic scattering and Stark relaxation in He + ThO collisions calculated using the *ab initio* DMS (Sec. II A) are almost identical to those calculated using the asymptotic approximation (21), in which the DMS is replaced by the permanent dipole moment of the isolated ThO molecule. These results justify the use of the asymptotic approximation in quantum scattering calculations of helium–molecule collisions in the presence of an external electric field.

ACKNOWLEDGMENTS

This work was supported by the Chemical Science, Geoscience, and Bioscience Division of the Office of Basic Energy Science, Office of Science, U.S. Department of Energy and NSF grants to the Harvard-MIT Center for Ultracold Atoms and the Institute for Theoretical Atomic, Molecular and Optical Physics at Harvard University and the Smithsonian Astrophysical Observatory. A.A.B. and E.R.S. acknowledge support from the Russian Basic Research Fund (project 08-03-00414) and from Moscow State University.

APPENDIX: INTERACTION OF COLLISION COMPLEX WITH AN EXTERNAL ELECTRIC FIELD

The term neglected in the derivation of Eq. (21) can be written in the form

$$-\mathbf{E}\cdot\mathbf{d}(R,\theta) = -Ed_z(R,\theta)\cos\theta_r, \tag{A1}$$

where θ_r is the angle between $\mathbf{r}$ and the electric field vector $\mathbf{E}$. The *ab initio* calculations presented in Sec. IIA indicate that only the parallel component of the DMS in the direction of the ThO axis is different from zero. Expanding this component in Legendre polynomials

$$d_z(R,\theta) = \sum_\lambda d_\lambda(R) P_\lambda(\cos\theta) \tag{A2}$$

and using the spherical harmonics addition theorem,[27] we obtain

$$d_z(R,\theta)\cos\theta_r = \sum_\lambda d_\lambda(R)\frac{4\pi}{2\lambda+1}\sum_{m_\lambda} Y^\star_{\lambda m_\lambda}(\mathbf{R}) Y_{\lambda m_\lambda}(\mathbf{r})\cos\theta_r. \tag{A3}$$

The product $Y_{\lambda m_\lambda}(\mathbf{r})\cos\theta_r$ can be expanded in a Clebsch–Gordan series[27]

$$Y_{\lambda m_\lambda}(\mathbf{r})\cos\theta_r = (2\lambda+1)^{1/2}\sum_{\tilde\lambda=|\lambda-1|}^{\lambda+1}(-1)^{m_\lambda}(2\tilde\lambda+1)^{1/2} \times \begin{pmatrix}\lambda & 1 & \tilde\lambda\\ 0 & 0 & 0\end{pmatrix}\begin{pmatrix}\lambda & 1 & \tilde\lambda\\ m_\lambda & 0 & -m_\lambda\end{pmatrix} Y_{\tilde\lambda -m_\lambda}(\mathbf{r}). \tag{A4}$$

Combining Eqs. (A3) and (A4) and evaluating the angular integrals, we obtain the molecule-field interaction matrix elements in the fully uncoupled basis defined in Sec. III A 2

$$\begin{aligned}\langle jm_j|\langle lm_l| - Ed_z(R,\theta)\cos\theta_r|j'm'_j\rangle|l'm'_l\rangle &= -E\sum_\lambda d_\lambda(R)\sum_{m_\lambda}(-)^{m_l+m_j}[(2l+1)(2l'+1)]^{1/2}\\ &\times[(2j+1)(2j'+1)]^{1/2}\begin{pmatrix}l & \lambda & l'\\ 0 & 0 & 0\end{pmatrix}\begin{pmatrix}l & \lambda & l'\\ -m_l & -m_\lambda & m'_l\end{pmatrix}\\ &\times\sum_{\tilde\lambda=|\lambda-1|}^{\lambda+1}(2\tilde\lambda+1)^{1/2}\begin{pmatrix}\lambda & 1 & \tilde\lambda\\ 0 & 0 & 0\end{pmatrix}\begin{pmatrix}j & \tilde\lambda & j'\\ 0 & 0 & 0\end{pmatrix}\\ &\times\begin{pmatrix}\lambda & 1 & \tilde\lambda\\ m_\lambda & 0 & -m_\lambda\end{pmatrix}\begin{pmatrix}j & \tilde\lambda & j'\\ -m_j & m_\lambda & m'_j\end{pmatrix}.\end{aligned} \tag{A5}$$

We have carried out test calculations based on Eq. (A5) using the *ab initio* DMS for He–ThO calculated as described in Sec. II A. Figure 14 compares the cross sections for elastic scattering and Stark relaxation in He + ThO collisions calculated using the full DMS (dashed line) and the asymptotic approximation (21) for the molecule–field interaction. The results obtained using the asymptotic approximation are in very good agreement with exact calculations over the range of collision energies of 0.01–2 cm^{-1}. We conclude that Eq. (21) is an excellent approximation for collision energies above 0.01 cm^{-1} and electric fields below 100 kV/cm.

[1] L. D. Carr, D. DeMille, R. V. Krems, and J. Ye, New J. Phys. **11**, 055049 (2009); M. T. Bell and T. P. Softley, Mol. Phys. **107**, 99 (2009).
[2] J. M. Doyle, B. Friedrich, J. Kim, and D. Patterson, Phys. Rev. A **52**, R2515 (1995).
[3] R. Côté, M. J. Jamieson, Z.-C. Yan, N. Geum, G.-H. Jeung, and A. Dalgarno, Phys. Rev. Lett. **84**, 2806 (2000); A. Derevianko, R. Cote, A. Dalgarno, and G.-H. Jeung, Phys. Rev. A **64**, 011404(R) (2001).
[4] S. E. Maxwell, N. Brahms, R. deCarvalho, D. R. Glenn, J. S. Helton, S. V. Nguyen, D. Patterson, J. Petricka, D. DeMille, and J. M. Doyle, Phys.

Rev. Lett. **95**, 173201 (2005); D. Patterson and J. M. Doyle, J. Chem. Phys. **126**, 154307 (2007); D. Patterson, J. Rasmussen, and J. M. Doyle, New J. Phys. **11**, 055018 (2009).
[5]A. C. Vutha, W. C. Campbell, Y. Y. Gurevich, N. R. Hutzler, M. Parsons, D. Patterson, E. Petrik, B. Spaun, J. M. Doyle, G. Gabrielse, and D. DeMille, J. Phys. B **43**, 074007 (2010).
[6]A. A. Buchachenko, J. Chem. Phys. **133**, 041102 (2010).
[7]A. Volpi and J. L. Bohn, Phys. Rev. A **65**, 052712 (2002).
[8]R. V. Krems and A. Dalgarno, J. Chem. Phys. **120**, 2296 (2004).
[9]R. V. Krems, H. R. Sadeghpour, A. Dalgarno, D. Zgid, J. Kłos, and G. Chałasiński, Phys. Rev. A **68**, 051401(R) (2003).
[10]N. Balakrishnan, G. C. Groenenboom, R. V. Krems, and A. Dalgarno, J. Chem. Phys. **118**, 7386 (2003).
[11]S. M. Skoff, R. J. Hendricks, C. D. J. Sinclair, J. J. Hudson, D. M. Segal, B. E. Sauer, E. A. Hinds, and M. R. Tarbutt, Phys. Rev. A **83**, 023418 (2011).
[12]J. M. Hutson and F. R. McCourt, J. Chem. Phys. **80**, 1135 (1984); J. M. Hutson, J. Chem. Phys. **86**, 854 (1987).
[13]W.-K. Liu, F. R. W. McCourt, and A. S. Dickinson, Mol. Phys. **66**, 565 (1989).
[14]L. Monchik, K.-S. Yun, and E. A. Mason, J. Chem. Phys. **39**, 654 (1963); L. Monchik and S. Green, J. Chem. Phys. **63**, 2000 (1975).
[15]I. Roeggen, H. R. Skullerud, T. H. Lovaas, and D. K. Dysthe, J. Phys. B **35**, 1707 (2002).
[16]A. A. Buchachenko and N. F. Stepanov, Russ. J. Phys. Chem. **72**, 286 (1998) (in Russian).
[17]G. A. Parker and R. T Pack, J. Chem. Phys. **68**, 1585 (1978).
[18]R. Jochemsen, A. J. Berlinsky, and W. N. Hardy, Can. J. Phys. **62**, 751 (1984).
[19]H.-K. Chung and A. Dalgarno, Phys. Rev. A **66**, 012712 (2002).
[20]V. Aquilanti and F. Vecchiocattivi, Chem. Phys. Lett. **156**, 109 (1989).
[21]M.-J. Lu, K. S. Hardman, J. D. Weinstein, and B. Zygelman, Phys. Rev. A **77**, 060701(R) (2008); T. V. Tscherbul, A. A. Buchachenko, A. Dalgarno, M.-J. Lu, and J. D. Weinstein, Phys. Rev. A **80**, 040701(R) (2009).
[22]M.-J. Lu and J. D. Weinstein, New J. Phys. **11**, 055015 (2009).
[23]R. V. Krems and A. Dalgarno, in *Fundamental World of Quantum Chemistry*, edited by E. Kryachko and E. Brandas (Kluwer, Dordrecht, 2004), Vol. 3, Chap. 14, p. 273.
[24]N. R. Hutzler, M. Parsons, Y. V. Gurevich, P. W. Hess, E. Petrick, B. Spaun, A. C. Vutha, D. DeMille, G. Gabrielse, and J. M. Doyle (2011), e-print arXiv:1101.4217v1 [physics.atom-ph].
[25]W. A. Lester Jr., in *Dynamics of Molecular Collisions*, edited by W. H. Miller (Plenum, New York, 1976).
[26]A. M. Arthurs and A. Dalgarno, Proc. R. Soc. London, Ser. A **256**, 540 (1960).
[27]R. N. Zare, *Angular momentum* (Wiley, New York, 1988).
[28]M. D. Rowe and A. J. McCaffery, Chem. Phys. **43**, 35 (1979).
[29]In Sec. IV B, we define the elastic cross section as that for the $|10\rangle \rightarrow |10\rangle$ transition. This definition is not the same as adopted in Sec. IV A, but is natural in the presence of an electric field, which splits the $|10\rangle$ and $|1, \pm 1\rangle$ rotational states. Throughout Sec. IV B, we continue to use j as a label for field-dressed rotational states, even though j is not a good quantum number in the presence of an electric field.
[30]T. V. Tscherbul and A. Dalgarno, J. Chem. Phys. **133**, 184104 (2010).
[31]Z. Pavlovic, T. V. Tscherbul, H. R. Sadeghpour, G. C. Groenenboom, and A. Dalgarno, J. Phys. Chem. A **113**, 14670 (2009).
[32]T. V. Tscherbul, J. Chem. Phys. **128**, 244305 (2008).
[33]E. A. Mason and T. R. Marrero, Adv. At. Mol. Phys. **6**, 155 (1970).
[34]D. A. Coobme, R. F. Snider, and B. C. Sanctuary, J. Chem. Phys. **63**, 3015 (1975); R. F. Snider, Int. Rev. Phys. Chem. **17**, 185 (1998).
[35]N. Brahms, T. V. Tscherbul, P. Zhang, J. Kłos, H. R. Sadeghpour, A. Dalgarno, J. M. Doyle, and T. G. Walker, Phys. Rev. Lett. **105**, 033001 (2010).
[36]G. Edvinsson and A. Lagerqvist, Phys. Scr. **30**, 309 (1984).
[37]C. T. Dewberry, K. C. Etchison, and S. A. Cooke, Phys. Chem. Chem. Phys. **9**, 4895 (2007).
[38]C. Hampel, K. Peterson, and H.-J. Werner, Chem. Phys. Lett. **190**, 1 (1992); J. D. Watts, J. Gauss, and R. J. Bartlett, J. Chem. Phys. **98**, 8718 (1993); P. J. Knowles and H.-J. Werner, Chem. Phys. Lett. **115**, 259 (1985).
[39]X. Cao, M. Dolg, and H. Stoll, J. Chem. Phys. **118**, 487 (2003).
[40]X. Cao and M. Dolg, J. Mol. Struct.: THEOCHEM **673**, 203 (2004).
[41]T. H. Dunning, Jr., J. Chem. Phys. **90**, 1007 (1989).
[42]S. M. Cybulski and R. R. Toczyłowski, J. Chem. Phys. **111**, 10520 (1999).
[43]D. E. Woon and T. H. Dunning, Jr., J. Chem. Phys. **100**, 2975 (1994).
[44]M. H. Alexander, J. Chem. Phys. **108**, 4467 (1998).
[45]MOLPRO, a package of *ab initio* programs designed by H.-J. Werner, P. J. Knowles, R. Lindh *et al.*, version 2009.1, Cardiff, UK, 2009.
[46]E. R. Sayfutyarova, A. A. Buchachenko, M. Hapka, G. Chałasiński, and M. M. Szczęśniak (unpublished).
[47]G. Delgado-Barrio and J. A. Beswick, in *Structure and Dynamics of Non-Rigid Molecular Systems*, edited by Y. G. Smeyers (Kluwer, Dordrecht, 1994), p. 203.
[48]A. A. Buchachenko, T. A. Grinev, J. Kłos, E. J. Bieske, M. M. Szczęśniak, and G. Chałasiński, J. Chem. Phys. **119**, 12931 (2003); R. L. Wilson, Z. M. Loh, D. A. Wild, E. J. Bieske, and A. A. Buchachenko, J. Chem. Phys. **121**, 2085 (2004).
[49]C. H. Townes and A. L. Schawlow, *Microwave Spectroscopy* (McGraw-Hill, New York, 1955).
[50]F. Reif, *Fundamentals of Statistical and Thermal Physics* (McGraw-Hill, New York, 1965).
[51]J. O. Hirschfelder, C. F. Curtiss, and R. B. Bird, *Molecular Theory of Gases and Liquids* (Wiley, New York, 1954).
[52]D. E. Manolopoulos, J. Chem. Phys. **85**, 6425 (1986).
[53]S. Green and P. Thaddeus, Astrophys. J. **191**, 653 (1974).
[54]H. Cybulski, R. V. Krems, H. R. Sadeghpour, A. Dalgarno, J. Kłos, G. C. Groenenboom, A. van der Avoird, D. Zgid, and G. Chałasiński, J. Chem. Phys. **122**, 094307 (2005).
[55]M. Cvitas, P. Soldan, J. M. Hutson, P. Honvault, and J. M. Launay, J. Chem. Phys. **127**, 074302 (2007).